Journal of Low Temperature Physics (2020) 199:330–338
https://doi.org/10.1007/s10909-020-02362-0

Toward 100,000-Pixel Microcalorimeter Arrays Using Multi-absorber Transition-Edge Sensors

S. J. Smith[1,2] · J. S. Adams[1,2] · S. R. Bandler[1] · S. Beaumont[1,2] · J. A. Chervenak[1] · A. M. Datesman[1,3] · F. M. Finkbeiner[1,4] · R. Hummatov[1,2] · R. L. Kelly[1] · C. A. Kilbourne[1] · A. R. Miniussi[1,2] · F. S. Porter[1] · J. E. Sadleir[1] · K. Sakai[1,2] · N. A. Wakeham[1,2] · E. J. Wassell[1,3] · M. C. Witthoeft[1,5] · K. Ryu[6]

Received: 31 July 2019 / Accepted: 24 January 2020 / Published online: 1 February 2020

Abstract
We report on the development of multi-absorber transition-edge sensors (TESs), referred to as 'hydras'. A hydra consists of multiple X-ray absorbers each with a different thermal conductance to a TES. Position information is encoded in the pulse shape. With some trade-off in performance, hydras enable very large format arrays without the prohibitive increase in bias and readout components associated with arrays of individual TESs. Hydras are under development for the next generation of space telescope such as Lynx. Lynx is a NASA concept under study that will combine a $<1''$ angular resolution optic with 100,000-pixel microcalorimeter array with energy resolution of $\Delta E_{\mathrm{FWHM}} \sim 3$ eV in the soft X-ray energy range. We present first results from hydras with 25-pixels for Lynx. Designs with absorbers on a 25 µm and 50 µm pitch are studied. Arrays incorporate, for the first time, microstrip buried wiring layers of suitable pitch and density required to readout a full-scale Lynx array. The resolution from the coadded energy histogram including all 25-pixels was $\Delta E_{\mathrm{FWHM}} = 1.66 \pm 0.02$ eV and 3.34 ± 0.06 eV at an energy of 1.5 keV for the 25 µm and 50 µm absorber designs, respectively. Position discrimination is demonstrated from parameterization of the rise-time.

Keywords Imaging spectroscopy · Transition-edge sensor · Position-sensitive detector

✉ S. J. Smith
stephen.j.smith@nasa.gov

Extended author information available on the last page of the article

1 Introduction

X-ray spectroscopy is a powerful tool for probing the physical nature of matter in the universe at temperatures $> 10^{5-6}$ K. Lynx is a NASA flagship mission concept currently under study that will provide answers into key scientific themes related to (1) the dawn of black-holes, (2) galaxy formation and evolution, and (3) stellar evolution and ecosystems [1]. The Lynx X-ray Microcalorimeter (LXM) is one of the main instruments, which will combine a sub-arcsecond X-ray optic, with 100,000-pixel microcalorimeter array (with $\Delta E_{\mathrm{FWHM}} < 3$ eV), and will provide exquisite imaging and spectroscopy capabilities.

The desire to implement a detector with 100,000 imaging elements introduces significant technical challenges. For example, if each of the 100,000 imaging elements required an individual TES, the extremely high density of wiring within the array would be impractical, and the physical space required to incorporate the bias circuit and readout components would be prohibitively large. We are pursuing position-sensitive detectors as a practical approach to enabling 100,000-pixel arrays (which comes with some trade with resolution). Our 'hydras' consist of a single transition-edge sensor (TES) connected to multiple X-ray absorbers [2–4]. The absorbers are connected to the TES by a thermal 'link'. The conductance of each link is tuned to give a different thermal time constant between each absorber and the TES. Each pixel (where we define a pixel as a single absorber in the hydra) has a different characteristic pulse shape and enables position discrimination. Even with up to 25-pixels per hydra, the high-density, sub-μm wide traces required to connect all the TESs within the array is challenging. We have developed a process to combine, high-yield, planarized multi-stack buried wiring layers from Massachusetts Institute of Technology Lincoln Laboratory (MIT/LL) with the NASA TES hydra. By combining 25-pixel hydras that incorporate buried wiring, with state-of-the-art microwave multiplexing [5], it becomes practical to realize a 100,000-pixel instrument within the engineering constraints of a satellite.

We have previously reported on prototype hydra designs with up to 20 pixels per TES [4]. In this paper we report on the design and performance of the first 25-pixel hydras incorporating buried wiring, which are being specifically optimized for LXM.

2 Hydra Designs for LXM

The current baseline LXM configuration [6] consists of a main array (MA) of 3456 hydras, each with 25 individual pixels on a 50 μm pitch (86,400 total pixels). The energy resolution goal is $\Delta E_{\mathrm{FWHM}} \sim 3$ eV at energies $E < 7$ keV. The MA will provide a field-of-view of 5′ where each pixel provides an angular resolution of 1″. The central 1′ region of the array will consist of 25-pixel hydras with each pixel on a 25 μm pitch (12,800 total pixels). This, enhanced main array (EMA), will provide 0.5″ imaging with $\Delta E_{\mathrm{FWHM}} \sim 2$ eV.

We have fabricated a series of test arrays that include both the 250 μm pitch hydras and 125 μm pitch hydras in the same array. The TES is a 20×25 μm Mo/Au bilayer with normal state resistance of $R_n \sim 20$ mΩ. The absorbers are 3.2-μm-thick electroplated Au and are cantilevered ~4 μm above the substrate, supported by pillar-shaped stems that make contact to the thermal links. The gaps between the pixels are 1.6 μm at the base of the absorbers and 5.2 μm at the top. The thermal links between the absorbers and the TES are $d = 310$ nm thick evaporated Au and are either $w = 1$ or 2 μm wide. The thermal conductance of a link at temperature T with length L is calculated from the Wiedemann–Franz relation $G = 24.5\ T\ (d\ w)/(\rho\ L)$ nW/K, where the resistivity of the metal link is $\rho = 0.67$ μΩ cm. Thus, L and w are adjusted to tune the thermal conductance of each link. We use the same finite-element-modeling approach discussed in Ref. [3] to design the links, calculate the pulse shapes and the noise properties of the hydra. In [4] we showed a hierarchical 'tree' layout of the internal links that uses a series of 'trunks' and 'branches' to connect the pixels. This makes the design easier to layout when there are a large number of pixels to connect to the TES. In this design, instead of connecting every pixel directly to the TES, groups of pixels are connected together by link 'branches', and these groups then connect to the TES from 1 of the pixels in the group via link 'trunks'. For these designs, pixels are arranged into 5 groups, each with 5 pixels. The thermal links were designed such that pixels in group 1 are the most strongly thermally connected to the TES and so have the fastest signals in the rising edge of the pulses, whereas group 5 is the most thermally decoupled from the TES and has pixels with slowest rising edges. Figure 1 (left) shows the link layout for an EMA hydra before the

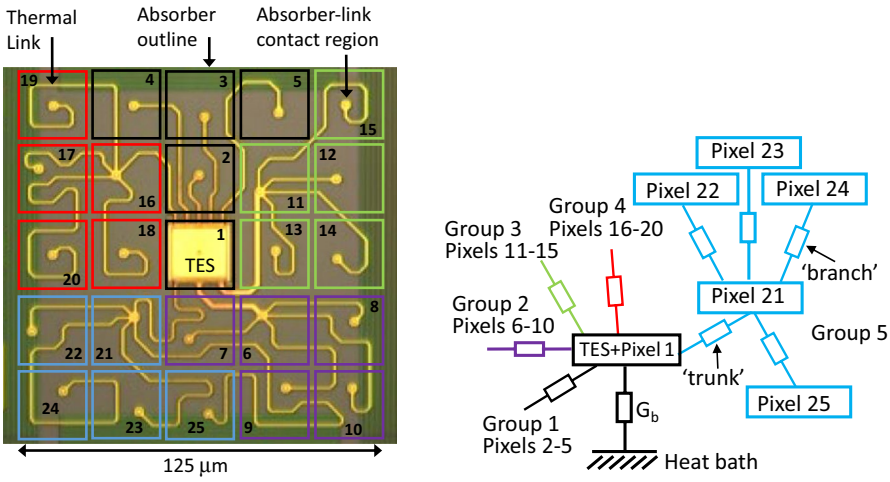

Fig. 1 Left, photograph of a 25-pixel hydra with 25 μm pitch absorbers for the LXM EMA. This image was before absorbers have been deposited to show the hierarchical link layout. The outline of where the absorbers are later deposited is indicated. Each group of 5 pixels is indicated in a different color. Pixels labeled 1–5 are group 1 (black), pixels 6–10 are group 2 (purple), pixels 11–15 are group 3 (green), pixels 16–20 are group 4 (red), and pixels 21–25 are group 5 (blue). Right, simplified thermal model showing part of the hydra 'tree' design. Groups of pixels are connected together by link 'branches', and these groups then connect to the TES via link 'trunks'. Only group 5 is shown in full (Color figure online)

absorbers have been deposited. Figure 1 (right) shows a simplified thermal model. The full trunk and branch structure are only shown for pixels 21–25, which constitute group 5. Figure 2 (left) shows a photograph of part of a test array including both 125 µm and 250 µm hydra designs. Figure 2 (right) shows a photo and cross-sectional schematic of how the TES connects to the buried microstrip Nb wiring layers using vias through the 200-nm-thick SiO_2 layers. The Nb traces are 200 nm thick and 500 nm wide. These are of suitable geometry to be able to wire a full-sized LXM array. Further details on the MIT/LL buried wiring fabrication process can be found in Refs. [6, 7]. We have previously used a high conductivity buried Cu layer in NASA developed substrates to improve heat-sinking and reduce thermal-cross-talk between pixels in the array [8]. We are currently developing a process to incorporate heat-sink layers into the MIT/LL substrates; however, this is not included on the arrays discussed here; thus, these devices are susceptible to additional noise from thermal cross-talk events.

3 Results

Measurements were taken in an Adiabatic Demagnetization Refrigerator (ADR) at the lowest operational bath temperature of $T_b = 47$ mK. The detectors were biased in their superconducting-to-normal transition at 2.5% R_n where the temperature of the TES is $T_0 \sim 50$ mK. The total heat capacity is $C(T_0) \sim 0.50$ pJ/K for the hydras with 50 µm pitch absorbers and $C(T_0) \sim 0.11$ pJ/K for the 25 µm pitch design. In both cases, this is dominated by the Au absorbers. From measurements of the TES bias power as a function of bath temperature, we estimate the differential thermal conductance ($G_b = dP/dT$) to the heat bath is $G_b(T_0) \sim 570$ pW/K and ~ 340 pW/K for the 50 µm and 25 µm designs, respectively. X-ray measurements were taken using a florescent Al-Kα (1.5 keV) target source. These initial measurements were taken using a relatively low total bias circuit inductance of ~ 20 nH. This provides a large electrical bandwidth and allows us to study the intrinsic thermal response of each

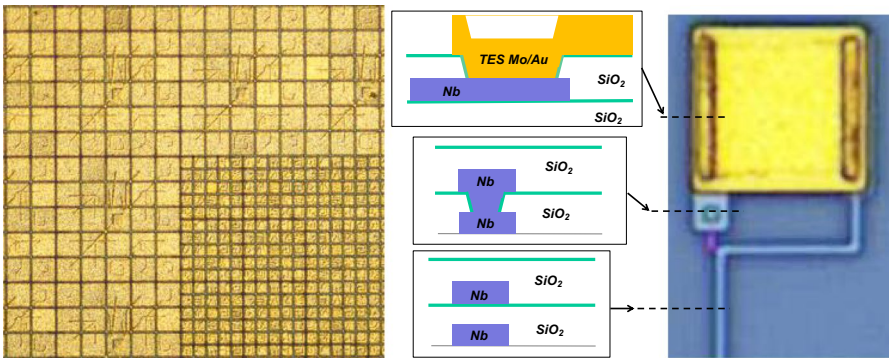

Fig. 2 Left, photograph of part of the LXM test array including 125 µm pitch EMA hydras in the central region of the array surrounded by a region of 250 µm pitch MA hydras. Right, photograph with cross-sectional schematic of buried wiring layer connections to Mo/Au TES (Color figure online)

hydra pixel to X-ray events. As such, the initial pulse rise-times are very fast. In order to multiplex many pixels, the rise-time must be slowed using higher circuit inductance. Slowing the rise-edge of the pulses relative to the white noise level of the readout chain has the potential to degrade the position discrimination. Although this has been accounted for in the hydra designs, the impact of higher circuit inductance on the position resolution needs to be experimentally verified and will be the subject of future studies. Because of the hierarchical layout of the link structure of these hydra designs, the pixel-dependent rising edge of the pulse signals has a complicated shape that cannot be uniquely characterized by a single rise-time calculation [4]. We are currently studying various techniques to extract position information from the pre-equilibration signal. Here we use a simple approach to parameterize the rising-edge of the pulse shapes using two metrics that extracts a fast and slow component to the rise-time. Figure 3 (left) shows a scatter plot of the rise-time calculated from the 10–50% point of the pulse height, versus the rise-time calculated from the 20–80% point after smoothing the pulses to suppress the faster component to the rise-time. The data are for the hydra design with 25 µm pitch absorbers. This simple analysis was sufficient to identify the 25 discrete populations of Al-Kα X-rays from which the average pulse shapes for each pixel in the hydra were determined. The ability to distinguish different pulse shapes is energy dependent because of two factors. Firstly, at lower energies the signal-to-noise ratio on the rise-time decreases (scaling as $1/E$); thus, the distributions become noisier. Secondly, at higher energies non-linearity in the pulse shape can introduce an energy dependence to the rise-time. Both of these effects can result in position confusion if neighboring rise-time populations overlap. The close proximity of the rise-time distributions for a few pixels with the fastest rise-times shown in Fig. 3 (left), suggests some overlap between distributions may occur at different X-ray energies. This preliminary algorithm is not rigorously optimized, and different approaches to characterizing the pre-equilibration signal will likely be required to determine the event position over a

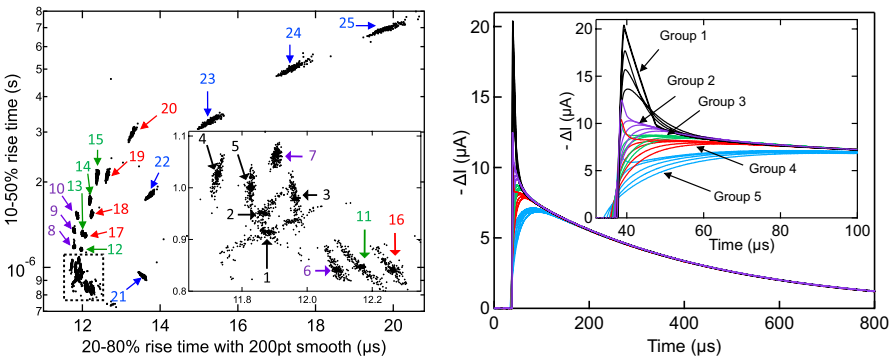

Fig. 3 Left, rise-time scatter plot for EMA hydra showing 25 separate regions that correspond to Al-Kα X-ray absorption in each of the 25-pixels. The inset shows a zoomed-in view of the region shown by a dashed box. The populations of events corresponding to each pixel are indicated on the figure. Right, average Al-Kα pulse shapes for each pixel in an EMA hydra. The inset shows a zoom-in of the first 60 µs, with the different groups of pixels identified (Color figure online)

broad range of energies. This is the subject of ongoing studies and will be reported at a later date. Figure 3 (right) shows the average measured pulse shapes for each pixel calculated from the population of events identified in the rise-time scatter plot. The pixel and group numbers are identified by comparing the measured pulse shapes with that modeled using the hydra design parameters. The inset shows a zoom-in of the first ~ 60 μs of the pulse shapes, which is the part of the signal where position information is encoded before all absorbers have come in to thermal equilibrium with each other. After this initial pre-equilibration time, the pulses decay to the baseline level with an exponential time constant of $\tau = 0.41$ ms.

A unique digital optimal filter is constructed for each pixel using the average measured Al-Kα pulse shapes. To calculate the pulse energy, a filter for a given pixel is applied to only the events attributed to absorption in that pixel [determined from Fig. 3 (left)]. Figure 4 (left) shows the coadded energy histogram for all 25 pixels of an EMA hydra for Al-Kα X-rays. The fitted resolution was $\Delta E_{\mathrm{FWHM}} = 1.66 \pm 0.02$ eV. This is consistent with the average of all pixels fitted individually, $\langle \Delta E_{\mathrm{FWHM}} \rangle = 1.68 \pm 0.13$ eV. Shown in Fig. 4 (right) is ΔE_{FWHM} from the individual energy histograms versus pixel number, illustrating a high degree of resolution uniformity. We note that in order to achieve the best ΔE_{FWHM} from pixels 1–3, an additional 5 kHz bandwidth limiting low-pass filter was applied to the digital optimal filter. We found this improved the average resolution of those pixels from 3.5 to 1.8 eV. A similar effect has been observed on other hydra designs [9] and has been attributed to event-to-event pulse shape variations in the rising edge of the pulses. The origin of this variation requires further study but could be due to position-dependence within an individual absorber (due to the finite thermal diffusion time). This will affect the pixels with the fastest rise-times (or largest signal bandwidth) the most. The high-frequency fluctuations in the signal can be suppressed by reducing the bandwidth of the optimal filter, which in turn enables better energy resolution [10]. Also shown in Fig. 4 (right) is the resolution calculated from the integration over frequency of the noise-equivalent

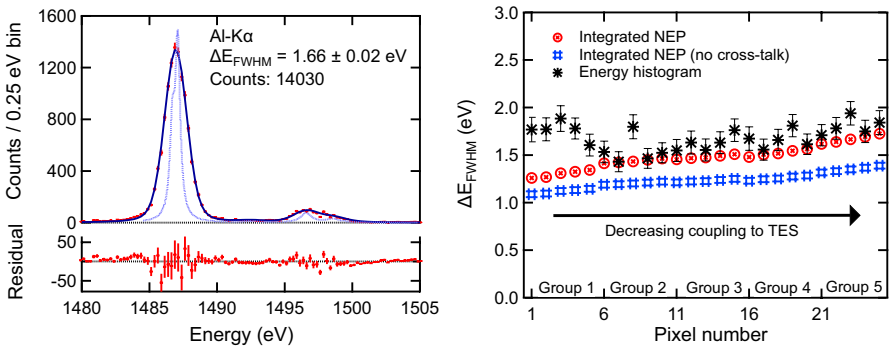

Fig. 4 Left, coadded Al-Kα energy histogram for all 25 pixels of an EMA hydra. The best fit gives $\langle \Delta E_{\mathrm{FWHM}} \rangle = 1.66 \pm 0.02$ eV. Right, ΔE_{FWHM} versus pixel, including that from individually fitted energy histograms (black stars), and the predicted resolution from the integrated *NEP*(*f*), measured both with (red circles) and without thermal cross-talk noise (blue boxes) (Color figure online)

power, *NEP*(*f*) [where *NEP*(*f*) is determined from measurements of the average pulse shape and noise spectral density]. To show the intrinsic *NEP*(*f*) for each pixel, we integrate over the full measurement bandwidth (155 kHz) without any additional low-pass filtering. The integrated *NEP*(*f*) degrades slightly as each group of pulses becomes more thermally decoupled from the TES. This is because the bandwidth of the pulse is reduced relative to the noise by the low-pass filtering from the links; thus, pixels in group 1 have better integrated *NEP*(*f*) compared to pixels in group 5. By comparing the integrated *NEP*(*f*) calculated using noise measured with and without X-rays illuminating the array [shown in Fig. 4 (right)], we estimate that thermal cross-talk noise degrades the resolution by about 20% at the measurement count-rate of ~ 1.5 cps. Thus, it is reasonable to assume that for future designs with optimized heat-sinking layers, improved ΔE_{FWHM} may be achievable. Because the resolution degradation due to cross-talk noise is proportional to E, we have not taken high statistics measurements at Mn-Kα (5.9 keV). However, low statistic measurements showed the average of the integrated *NEP*(*f*) without the thermal cross-talk was 1.55 eV. This compares to 1.23 eV at Al-Kα and suggests that once the heat-sinking has been incorporated, ΔE_{FWHM} should be close to meeting the 2 eV design goal for energies up to 7 keV.

Similar preliminary tests have been carried out on a MA hydra with 50 µm pitch absorbers. These larger hydras have ~ 5 times the heat capacity of the EMA equivalents, and the resolution should be approximately 2.5 times worse (since $\Delta E_{\mathrm{FWHM}} \propto \sqrt{C}$). Thus, in the absence of any excess cross-talk noise we expect the detector performance to be around 3 eV. We measured $\Delta E_{\mathrm{FWHM}} = 3.34 \pm 0.02$ eV from the coadded energy spectrum for all 25 pixels for Al-Kα X-rays (Fig. 5). In this measurement, the cross-talk noise is estimated to degrade the average resolution by ~ 20%, suggesting that ~ 3 eV could be achievable for a fully optimized device. The average measured pulse shapes are shown in Fig. 5 (right).

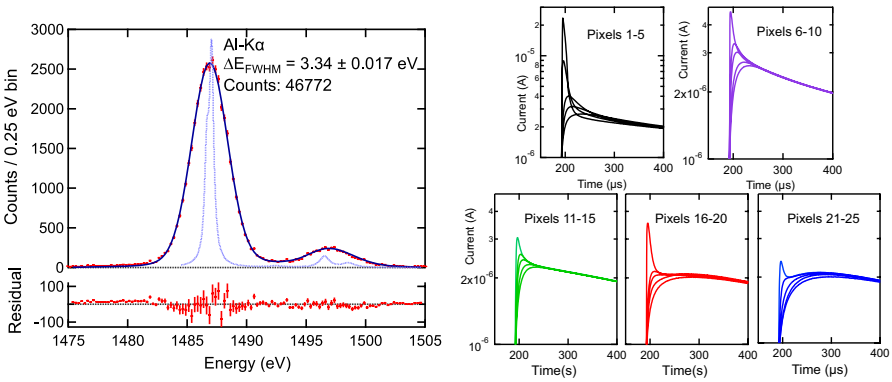

Fig. 5 Left, coadded Al-Kα energy histogram for all 25 pixels of an MA hydra. The best fit gives $\Delta E_{\mathrm{FWHM}} = 3.34 \pm 0.02$ eV and the average of the individually fitted histograms was $\langle \Delta E_{\mathrm{FWHM}} \rangle = 3.37 \pm 0.31$ eV. Right, average measured pulse shapes for each of the 5 groups of pixels (Color figure online)

4 Conclusion

We have demonstrated the first results from 25-pixel hydras that include buried wiring layers. The initial designs are of suitable pixel and wiring pitch for a full-sized LXM array and demonstrate the feasibility of making a 100,000-pixel instrument. Despite the lack of metallic heat-sinking layers, these pixels demonstrated excellent energy resolution and the ability to distinguish all 25-pixels for hydras with 25 μm and 50 μm pitch absorbers for 1.5 keV X-rays. Broad-band measurements are now required to study the energy resolution and position discrimination over the full LXM energy range (0.3–7 keV).

Acknowledgements MIT Lincoln Laboratory portion of the work is based upon work supported by the United States Air Force under Air Force Contract No. FA8702-15-D-0001. Any opinions, findings, conclusions or recommendations expressed in this material are those of the author(s) and do not necessarily reflect the views of the United States Air Force.

References

1. J.A. Gaskin, D. Swartz, A.A. Vikhlinin, F. Özel, K.E.E. Gelmis, J.W. Arenberg, S.R. Bandler, M.W. Bautz, M.M. Civitani, A. Dominguez, M.E. Eckart, A.D. Falcone, E. Figueroa-Feliciano, M.D. Freeman, H.M. Günther, K.A. Havey Jr., R.K. Heilmann, K. Kilaru, R.P. Kraft, K.S. McCarley, R.L. McEntaffer, G. Pareschi, W.R. Purcell, P.B. Reid, M.L. Schattenburg, D.A. Schwartz, E.D. Schwartz Sr., H.D. Tananbaum, G.R. Tremblay, W.W. Zhang, J.A. Zuhone, J. Astron. Telesc. Instrum. Syst. **5**(2), 021001 (2019). https://doi.org/10.1117/1.JATIS.5.2.021001
2. S.J. Smith, S.R. Bandler, R.P. Brekosky, A.-D. Brown, J.A. Chervenak, M.E. Eckart, F.M. Finkbeiner, N. Iyomoto, R.L. Kelley, C.A. Kilbourne, F.S. Porter, J.E. Sadleir, E. Figueroa-Feliciano, IEEE Trans. Appl. Supercond. **19**(3), 451–455 (2009). https://doi.org/10.1109/TASC.2009.2019557
3. S.J. Smith, Nucl. Instrum. Methods Phys. Res. Sect. A **602**(2), 537–544 (2009). https://doi.org/10.1016/j.nima.2009.01.158
4. S.J. Smith, J.S. Adams, S.R. Bandler, J.A. Chervenak, A.M. Datesman, M.E. Eckart, F.M. Finkbeiner, R. Hummatov, R.L. Kelley, C.A. Kilbourne, A.R. Miniussi, F.S. Porter, J.E. Sadleir, K. Sakai, N.A. Wakeham, E.J. Wassell, J. Astron. Telesc. Instrum. Syst. **5**(2), 021008 (2019). https://doi.org/10.1117/1.JATIS.5.2.021008
5. D. Bennett, B. Mates, S.R. Bandler, D.T. Becker, J.W. Fowler, J.D. Gard, G.C. Hilton, K.D. Irwin, K.M. Morgan, C.D. Reintsema, K. Sakai, D. Schmidt, S.J. Smith, D.S. Swetz, J.N. Ullom, L.R. Vale, A.L. Wessels, J. Astron. Telesc. Instrum. Syst. **5**(2), 021007 (2019). https://doi.org/10.1117/1.JATIS.5.2.021007
6. S.R. Bandler, J.A. Chervenak, A.M. Datesman, A.M. Devasia, M. DiPirro, K. Sakai, S.J. Smith, T.R. Stevenson, W. Yoon, D. Bennett, B. Mates, D. Swetz, J.N. Ullom, K.D. Irwin, M.E. Eckart, E. Figueroa-Feliciano, D. McCammon, K. Ryu, J. Olson, B. Zeiger, J. Astron. Telesc. Instrum. Syst. **5**(2), 021017 (2019). https://doi.org/10.1117/1.JATIS.5.2.021017
7. S.K. Tolpygo, V. Bolkhovsky, T.J. Weir, L.M. Johnson, M.A. Gouker, W.D. Oliver, IEEE Trans. Appl. Supercond. **25**, 1101312 (2015). https://doi.org/10.1109/TASC.2014.2374836
8. F.M. Finkbeiner, C.N. Bailey, S.R. Bandler, R.P. Brekosky, A.-D. Brown, J.A. Chervenak, M.E. Eckart, R.L. Kelley, D.P. Kelly, C.A. Kilbourne, F.S. Porter, J.E. Sadleir, S.J. Smith, IEEE Trans. Appl. Supercond. **21**(3), 223–226 (2011). https://doi.org/10.1109/TASC.2010.2091237
9. S.J. Smith, S.R. Bandler, R.P. Brekosky, A.-D. Brown, J.A. Chervenak, M.E. Eckart, F.M. Finkbeiner, R.L. Kelley, C.A. Kilbourne, F.S. Porter, E. Figueroa-Feliciano, Space telescopes and instrumentation 2008: ultraviolet to gamma ray, in *Proceedings of the Society of Photo-optical Instrumentation Engineers* (*SPIE*), vol. 7011, ed. by M.J.L. Turner, K.A. Flanagan, article 701126 (2008). https://doi.org/10.1117/12.790100
10. T. Saab, E. Figueroa-Feliciano, N. Iyomoto, S.R. Bandler, J.A. Chervenak, R.L. Kelley, C.A. Kilbourne, F.S. Porter, J.E. Sadleir, J. Appl. Phys. **102**(10), 104502 (2007). https://doi.org/10.1063/1.2811882

Affiliations

S. J. Smith[1,2] · J. S. Adams[1,2] · S. R. Bandler[1] · S. Beaumont[1,2] · J. A. Chervenak[1] · A. M. Datesman[1,3] · F. M. Finkbeiner[1,4] · R. Hummatov[1,2] · R. L. Kelly[1] · C. A. Kilbourne[1] · A. R. Miniussi[1,2] · F. S. Porter[1] · J. E. Sadleir[1] · K. Sakai[1,2] · N. A. Wakeham[1,2] · E. J. Wassell[1,3] · M. C. Witthoeft[1,5] · K. Ryu[6]

1 NASA Goddard Space Flight Center, Greenbelt, MD, USA

2 Center for Research and Exploration in Space Science and Technology, University of Maryland Baltimore County, Baltimore, MD, USA

3 Science Systems and Applications Inc., Lanham, MD, USA

4 Sigma Space Corporation, Lanham, MD, USA

5 ADNET Systems, Inc., Bethesda, MD, USA

6 MIT Lincoln Laboratory MIT, 244 Wood Street, Lexington, MA, USA